Compressible Flow Structures Interaction with a 2-D Ejector: A Cold-Flow Study

H. Zare-Behtash* and K. Kontis†

School of MACE, The University of Manchester, M60 1QD, UK

Abstract

An experimental study has been conducted to examine the interaction of compressible flow structures such as shocks and vortices with a 2-D ejector geometry using a shock tube facility. Three diaphragm pressure ratios of $P_4/P_1 = 4$, 8, and 12 have been employed, where P_4 is the driver gas pressure and P_1 is the pressure within the driven compartment of the shock tube. These lead to incident shock Mach numbers of $M_s = 1.34$, 1.54, and 1.66, respectively. The length of the driver section of the shock tube was 700 mm. Air was used for both the driver and driven gases. High-speed shadowgraphy was employed to visualise the induced flow field. Pressure measurements were taken at different locations along the test section to study the flow quantitatively. The induced flow is unsteady and dependent on the degree of compressibility of the initial shock wave generated by the rupture of the diaphragm.

*Research Student, School of MACE, The University of Manchester, UK. AIAA Student Member

†Professor (Reader), School of MACE, The University of Manchester, UK. AIAA Senior Member

I. INTRODUCTION

Studies of shocks expanding into confined regions lack detailed quantitative data of major flow-field features that evolve in time. The transient behaviour of shock waves and detonations has been the subject of study of many investigations. These include phenomena such as shock reflection, diffraction and shock/vortex interactions. Shock wave reflections have been studied both experimentally and analytically by Ben-Dor et al.[1,2] and Henderson et al.[3] The shock diffraction pattern over corners at different Mach numbers has been studied experimentally by Skews[4,5] and Griffith et al.[6] Shock diffraction from small to larger areas, has been studied by a number of authors such as Chang and Kim[7] and Jiang et al.[8] The main focus of these studies has only been a specific aspect of shock wave behaviour, i.e., diffraction, reflection, or shock/vortex interaction.

Detonation diffractions from small to larger areas have especially attracted the attention of many researchers. Detonations are distinguished from shock waves by the presence of an intrinsic length scale associated with a reaction zone.[9–11]The study into the evolution of detonation waves that suddenly expand has been motivated not only by the need to suppress accidental detonations but also in the interest of the applicability of such flows to the concept of Pulse Detonation Engines (PDEs).[12–19]

Pulse detonation engines are currently being investigated as a new technology for aerospace propulsion.[20] Because of the inherently unsteady nature of PDEs, one of the main challenges to making practical engines is minimising the losses at the inlet and outlet. Ejectors are fluid pumps that are used to entrain secondary flows using a primary flow. For propulsion applications, this entrainment can augment thrust compared to that generated by the primary flow alone and thereby increase performance. Of course high thrust augmentation for PDE-ejector applications is only achievable once the gas-dynamics and the flow interactions of the PDE-ejector system are understood.[21]

Non-detonational computational studies have highlighted the importance of the starting vortices, precursor shocks, and direct pressure loads created by the gas-dynamic (shock-tube) processes within the ejector to the overall thrust-augmentation performance of the system. These data will be valuable for calibrating computational fluid dynamics codes and ultimately for the optimisation of PDE-ejector configurations for propulsion applications.[22]

The present study examines both qualitatively and quantitatively the interaction of compressible structures such as shocks and vortices with a 2-D ejector configuration. These structures are generated by the passage of shock waves through a converging nozzle with an ejector placed at the exit. The interaction of the flow features with the test section generates multiple shock waves which travel both upstream and downstream. The behaviour of these shocks will have a significant impact in the performance of multi-cycle PDEs, especially on parameters related to the purging period where adequate pressure levels are vital[23] and where convergent nozzles are used at the nozzle exit to preserve chamber pressure. The presence of these shocks also plays an important role in the noise levels produced by PDEs which must meet standard noise regulations.[24]

II. EXPERIMENTAL SETUP

Experiments have been carried out using a cylindrical shock-tube, made of seamless pipe to generate the shock waves. The internal and external diameters of the shock-tube were 30 mm and 38 mm, respectively. Driver gas pressures of $P_4 = 4$, 8 and 12 bar were examined, with the pressure in the driven section (P_1) being ambient. Air has been used as both the driver and driven gases. Using Eq. (1) the driver pressures correspond to theoretical Mach numbers of $M_s = 1.31$, 1.49 and 1.61, respectively.[25]

$$\frac{P_4}{P_1} = \left[1 + \frac{2\gamma_1}{\gamma_1 + 1}\left(M_s^2 - 1\right)\right]\left[\frac{1}{1 - \frac{\gamma_4 - 1}{\gamma_1 + 1}\frac{a_1}{a_4}\left(M_s - \frac{1}{M_s}\right)}\right]^{\frac{2\gamma_4}{\gamma_4 - 1}} \tag{1}$$

Where M_s is the incident shock Mach number, γ is the ratio of specific heats, and a is the velocity of sound. The subscripts 1 and 4 correspond to the driver and driven gases, respectively.

The driver length was 700 mm. An industrial film diaphragm divided the two sections of the shock tube. The thickness of the diaphragm used was 23, 55 and 75μm for $P_4/P_1 = 4$, 8 and 12, respectively. This is the minimum thickness which can sustain the desired pressure without spontaneously rupturing. The bursting of the diaphragm was initiated manually with a plunger. The setup is similar to that described by References $25 - 27$.

In order to study the different aspects of shock wave behaviour, the model shown in Figure 1 was employed.[28] This is attached to the circular shock tube via an adaptor which gradually

changes the nozzle shape from circular to rectangular, allowing for the two-dimensional study of the flow.[29] A similar approach has been employed by Allgood et al.[22] in order to produce a $2-D$ test section. The test section is divided into three parts. As the shock wave enters the test section, it first encounters a concave surface converging into an area of uniform cross-section with a contraction ratio of $6:1$ and a throat height of $H = 9.6\ mm$. The shock then diffracts into a region bounded by solid straight walls on the top and bottom surfaces representing the ejector walls. The test section had a nominal width of $2 \times H$.

Optical grade perspex sheets with a thickness of 10 mm were used on both sides of the nozzle to allow the visualisation of the flow. The reason for choosing the relatively thick perspex sheets was due to the high pressures encountered during the experiments. In order to maintain a good seal between the nozzle geometry and the perspex sheets on either side, a thin layer of *Hermatite* instant rubber gasket was applied on the nozzle walls. The instant gasket has a high pressure and temperature tolerance providing an ideal seal.

High-speed shadowgraphy[30] was employed to visualise the flow. Although a qualitative technique, shadowgraphy can offer great insight into the fluid dynamic structure of the flow. Pictures were captured, in time sequence, by delaying the triggering of the light source using a signal synchronisation unit.

The Shimadzu Hyper-Vision camera was also utilised to produce a motion picture of the flow field. Illumination for the Shimadzu camera was provided via a 300 W continuous Xenon lamp, and the optical arrangement was identical to the shadowgraphy setup with the exception of the light source.

Wall pressure measurements were conducted by placing a number of transducers along both the upper and lower confining walls of the ejector and also on the side wall of the chamber. Their location are marked in Figure 1. Transducers $T1$ to $T5$ are positioned along the side wall, while transducers $T6$ and $T7$ were placed on the upper and lower ejector walls. The side wall transducers were placed 40 mm from each other with the first transducer placed 10 mm from the entrance of the test section. Transducer $T6$ is located 20 mm downstream of the exit of the uniform area section with transducer $T7$ placed 40 mm further down. The transducers were calibrated using a deadweight tester.[31] The data were recorded and stored by means of a high-speed data acquisition system (National Instruments $PCI-6251$), via a signal conditioner (National Instruments $SCXI-1520$). The system had the capability of collecting data at a frequency up to 50 kHz. The stored data were then processed using

Matlab.

The repeatability error was found to be approximately ±4% for the shadowgraphs. This was calculated by taking three images having identical time delays and comparing the distance that the shock wave has moved relative to the entrance of the test section. This takes into account: (i) setting the same driver pressure, (ii) having the same delay time output from the delay generator, and (iii) triggering the light source to capture an image.

The pressure readings presented are the average of three test runs performed for each driver pressure. For each pressure measurement, a total of 20000 data points were collected over a period of 0.5 seconds. The repeatability of the pressure readings was deduced by comparing every $2000th$ point of the data range collected for three randomly chosen transducers. This gave a maximum error of 1%. In all the error calculations, the mean value was used to compare the offset of the individual values.[32]

III. RESULTS AND DISCUSSION

A. Effect of Area Change

Chisnell[33] derived a first order relationship between changes in area and shock strength for a shock moving through a small area change. He found that:

$$Af(z) = \text{constant} \tag{2}$$

where A is the area, and the Chisnell function $f(z)$ is given in Eq. (3) in terms of the shock strength $z = p_2/p_1$, p_2 and p_1 being the pressures upstream and downstream of the shock, and the specific heat ratio, γ.

$$f(z) = z^{1/\gamma}(z-1)\left(z+\frac{\gamma-1}{\gamma+1}\right)^{-1/2}$$
$$\times\left[\frac{1+\left\{1+\frac{(\gamma+1)}{(\gamma-1)z}\right\}^{-1/2}}{1-\left\{1+\frac{(\gamma+1)}{(\gamma-1)z}\right\}^{-1/2}}\right]^{\sqrt{\gamma/2(\gamma-1)}}$$
$$\times\left[\frac{\left\{1+\frac{(\gamma+1)}{(\gamma-1)z}\right\}^{-1/2}-\left(\frac{\gamma-1}{2\gamma}\right)^{1/2}}{\left\{1+\frac{(\gamma+1)}{(\gamma-1)z}\right\}^{-1/2}+\left(\frac{\gamma-1}{2\gamma}\right)^{1/2}}\right]$$
$$\times exp\left[\left(\frac{2}{\gamma-1}\right)^{1/2} tan^{-1}\left\{\frac{2}{\gamma-1}\left(\frac{\gamma z}{z+\frac{\gamma+1}{\gamma-1}}\right)^{1/2}\right\}\right]. \quad (3)$$

Given the value of the shock strength on encountering an area change and the ratio of the areas at the ends of the variable area section, the strength of the shock emerging from this section is obtained from Eqs. (2) and (3).

As the shock enters the rectangular inlet of the test section from the circular shock tube, its strength increases by 5.5%, 6.6%, and 8.1% respectively for $P_4/P_1 = 4$, 8 and 12 due to the area reduction of 22%.

Discrepancies risen between this theoretical analysis and experimental results may be attributed to the disturbances generated by the motion of the incident shock. As these disturbances move through the non-uniform medium behind the shock, their strengths change and further disturbances are reflected which move through the fluid in the same direction as the shock. This was shown to be the case in the experimental studies performed by Bird.[34] The strength of a shock wave in an area change is non-uniform, but can be assigned an average value, predicted by Chisnell's theory. In a situation where the strength varies rapidly along the shock front, this bears little relevance to the true unsteady shock strength at a given point on the front. The average value approximates to the unsteady strength only when applied to a portion of the shock front across which the strength is not changing rapidly.[35]

B. Converging-Concave Section

As the incident shock travels along the concave surface it is again strengthened by the area reduction of the converging nozzle and becomes even stronger.[22,33–36] The physical processes

occurring in a gas behind a shock wave lead to a noticeable change in flow pattern, more intensive reflected waves and higher flow turbulence. Since there is always a certain degree of roughness on even the very smooth walls of the test section, the flow structure behind the wave is defined by micro disturbances that exist on the walls. As a result of superposition of such patterns from many random disturbances on the wall, the flow structure behind the shock wave will be made up from the following disturbance mesh (Figure 2): lines of tangential discontinuities (I), transverse sonic waves (II), and the mesh of Mach lines for the case of supersonic flow (III). As stated by Korobeinikov,[37] the visibility of the different disturbances depends strongly on the apparatus used to visualise the flow. For example if the Schlieren method is used with a vertical knife edge, the incident wave and the Mach-line mesh become prominent, and when the knife edge is horizontal, the transverse waves stand out clearly. Because in our case shadowgraphy has been used we would have expected all the flow features as shown in Figure 2(b) to be noticeable. However, the lack of adequate spatial resolution in the present study is due to the relative thick sheets of perspex windows.

Previous studies have reported that a regular reflection (RR) transitions into an irregular reflection (IR) with increase in the effective wedge angle, and vice-versa. The reflection of a planar shock wave over a concave surface goes through four sequence of events; a direct Mach reflection, $DiMR$, in which the triple point moves away from the reflecting surface, a momentarily stationary Mach reflection, $StMR$, where the triple point moves parallel to the reflecting surface, an inverse Mach reflection, $InMR$, where the triple point moves towards the reflecting surface, and finally termination of the $InMR$ and the formation of RR. Since the RR configuration, formed after the termination of an $InMR$, has a special structure associated with it, it is referred to as a transitioned regular reflection TRR. The reflection process over a concave wedge can be summarised as follows:[38]

$$DiMR \rightarrow StMR \rightarrow InMR \rightarrow TRR.$$

C. Uniform Area Section

As the transitioned regular reflection pattern moves along the channel, as shown in Figure 3 for the $P_4/P_1 = 12$ case, the reflected waves that were once part of the Mach reflection (discussed in Sect. III B), move towards each other and collide head on. As the reflected waves pass each other they create two focal points, one at the front just behind the incident

shock and the other at the rear just before the entrance into the concave section. These waves then move towards the channel walls and are again reflected from them. The head-on collision, passing and reflecting from the walls, like a bouncing motion, is continuously repeated and gives rise to an even more complicated structure.

The location where the reflected wave is attached to the incident shock wave varies as the flow travels further downstream. At one instant the reflected and incident shock waves make contact along the surface of the channel, giving rise to a regular reflection pattern, while at a later time this attachment point moves along the incident wave away from the wall as the reflected and incident shocks merge at the stem of the newly formed Mach reflection. The wave reflecting from the opposite wall behaves in a similar manner. The development of the Mach reflection depends on the competition between the convergence of the reflected waves from the walls and acceleration of the shock on the centre-line which determines whether the three-shock intersections cross or remain un-crossed. The slip stream formed in Mach reflection causes the flow to separate and a vortex forms along the wall.[39,40] This pattern is repeated on the opposite surface, which explains the pair of vortices visible behind the incident shock in Figure 3.

D. Diffraction Region

When the shock wave pattern reaches the end of the constant area nozzle, a diffraction occurs, i.e., turning of the wave around the vertex. The diffraction pattern for a driver pressure ratio of 8 is given in Figure 4(a), with the schematic of the diffraction pattern shown in Figure 4(b). In Figure 4(b) AN is the diffracted shock wave, ARO is the front of the reflected expansion wave which propagates back into the oncoming flow, AL is the contact surface which separates that part of the flow field processed by the diffracting shock wave from that processed by the incident wave.[41] During diffraction, one end of the contact surface bends around the vortex while it is attached to the incident wave at the other end.

Due to the increase in the surface area of the diffracted shock and the rapidly expanding flow in the gas behind the wall shock, the diffracted shock is attenuated.[35] Although the diffraction of the shock wave at a convex corner results in its distortion and the loss of its intensity, these changes are only experienced by that region of the shock front within which there is interaction with the centred rarefaction fan from the wedge apex.[42]

The reflected shock outlined in the shadowgraph of Figure 4(a) and represented by M in the schematic of Figure 4(b), are segments of the reflecting waves inside the uniform area section that bounce up and down continuously.

E. Overall Flow Analysis

Figure 5 shows the flow features described in our forthcoming analysis with some key features highlighted in the image. These include the formation of vortices from the nozzle exit due to baroclinic effects, shock reflections from the ejector walls by the consecutive diffracted shock waves, and finally the spade like shock structures formed by diffraction and focusing of the shocks upstream through the converging-concave section.

Figures 6, 7 and 8 represent the shadowgraph series of the events unfolded for driver pressure ratios of 4, 8, and 12, respectively. Each frame is labelled with the corresponding time, in milliseconds, relative to the time the shock front first appears in the test section. This happens to be the first frame in Figure 6. Since the initial phase of the flow at the two higher driver pressure is similar to the lower pressure case, the images of Figures 7 and 8 are chosen to focus more on the later stages of the flow.

Although the middle segment of the incident shock in Figure 6(a) is plane, the edges have undergone Mach reflection. This is inferred by the darkened regions at the point of contact between the shock wave and the section walls. As the transitioned regular reflection enters the uniform area section, the two reflected shocks cross-over and reflect from the opposite walls. The first crossing is evident in Figure 6(b).

The planar shock wave undergoes transition to a cylindrical shock front as it diffracts out of the nozzle and into the ejector (Figure 6(c)). The expansion of the shock due to the area change occurs in two phases. The axial shock strength (i.e., the shock front along the centreline axis) remains roughly constant before decreasing rapidly.[35,43] This is due to the fact that the shock remains planar until the 'critical shock' is reached. The critical shock is defined as the shock wave that first becomes fully non-planar (curved). In general the distance that a shock has to travel to attain symmetry decreases as the initial Mach number increases.

Two vortex cores of opposite circulation are formed at the corner of the area expansion and are convected downstream and expand outward slightly (Figure 6(c)–6(e)). For weak

incident shock waves, the vortex is nearly circular whereas for higher Mach numbers (Figures 7(a) and 8(a)) the vortex cores are stretched downstream, an observation consistent with the numerical work of Sun and Takayama.[44]

The segments of the bouncing reflected waves inside the uniform area section move backwards into the oncoming flow; these form a pattern which appear as a trail of spades (Figures 6(c), 7(a), and 8(a)). The features explained so far, both in the converging section and the uniform area section, are present for all three driver pressures.

The initial incident wave and the first set of reflected waves exiting the nozzle go through a regular reflection pattern upon collision with the wall as they develop a cylindrical shape. The diffracted cylindrical shock wave encounters the wall head on with an initial reflection angle of 90^o. As the shock wave propagates outwards the point where it touches the reflecting surface encounters an ever decreasing effective reflecting wedge angle, and the reflection type transitions to Mach reflection.[45–50] In Figures 6(e), 7(b) and 8(b) the Mach stem is clearly visible for the precursor shock front.

Once the precursor shock wave diffracts into the open channel the front attachment point between the reflected shock and the incident shock wave travels with it (see Figure 3). At the same time the rear attachment point moves further into the constant area channel. When this happens the shock focusing that occurs from the fusion of the two reflected shocks does not occur anymore and the shocks moving back into the oncoming flow start to fade away signalling the decay of the shock strength.[40] We can see this by comparing Figures 6(c) and 6(d) for driver pressure ratio of 4, Figures 7(a) and 7(b) for driver pressure ratio of 8, and Figures 8(a) and 8(c) for the driver pressure ratio of 12.

Another feature that is present in the current study is the presence of an embedded shock wave or a 'diaphragm shock'.[7] This is similar to the embedded shock within axisymmetric vortex rings in shock tube studies performed by authors such as: Baird,[51] Minota,[52] Broadbent and Moore,[53] and Kontis et al.[26] This shock is evident as a dark vertical line downstream of the nozzle exit in Figures 6(f) and 7(b), and forms once the original vortex cores have pinched off from the shear layer. For the highest driver pressure this shock wave does not appear to be stable for long, and dissipates due to the interaction between the shock reflection patterns that occur outside the uniform area nozzle.

In Figure 7(b) we see the result of the interaction between a shock wave and a vortex, namely, the phenomenon of 'shock splitting'.[54] The reflected shock waves from the upper

and lower walls of the ejector interact with the two vortex cores and their propagation is altered, an observation consistent with Ellzey et al.[55] Focusing on the lower vortex core which is rotating clockwise, we notice that the portion of the reflected shock wave to the right of the core travels more slowly; at the same time the portion of the reflected shock to the left of the core, which has just been reflected from the underside of the nozzle is also slowed down. The shock wave splitting phenomenon produces secondary shock waves which add to the complexity of our already intricate flow. This interaction is also visible in Figure 6(d), with its effects noticeable in Figures 8(b) and 8(c).

The overall flow structure is greatly influenced by the shock strength. This is due to the non-linear interactions of the many flow-field elements which are confined in a limited flow passage.[7] The number of waves behind the diffracted precursor shock wave increases as higher Mach numbers are explored (see Figure 8(a)). Each time a wave is diffracted from the uniform area section (as a consequence of the continuous bouncing motion of the two reflected waves within the section), a shock focusing also takes place which travels back into the oncoming flow. As far as shock-vortex interactions are concerned, weak interactions involve slight deformation of the shock and the acoustic wave generation whilst strong interactions involve significant deformation of the shock wave due to the vortex and may include the production of secondary shocks.[56]

As the incident shock reaches the uniform area section, a region of turbulent flow builds up at the entrance of the test section (Figures 7(a) and 8(a)). This region propagates downstream with time and is also more intense with increasing shock strength.[57] The turbulent region is believed to be generated because of the 1 mm step thickness that exists between the test section and the perspex sheets on either side. The motion of this turbulent region is limited by the upstream motion of the diffracted spade structures. As the spade structures approach the inlet of the test section, the precursor shock begins to flatten due to the high-speed opposing flow. By looking at Figures 8(a)–8(c) we see that the original convex to the left shock front has become almost planar. In Figure 6(c) this convex portion does not exist. The intermediate pressure ratio also has the same characteristics as the higher pressure ratio case.

Figure 9 presents the sequence of images taken by the Shimadzu Hyper-Vision camera at 125 $kfps$ for a diaphragm pressure ratio of 8. The time frames presented show the key stages of the flow development. Since the imaging was performed at a high rate, the quality

of the images is lower than the shadowgraphs. Following the sequence we see the reflected shocks of the three-shock Mach configuration approaching each other in Figure 9(a). The shocks pass one-another and are just about to make contact with the upper and lower walls in Figure 9(b). It is at this point where the trailing edges of the two reflected shocks first make contact with each other and begin to form the precursor front, convex to the left. The flow pattern that develops can be followed through the rest of the images. As the reflected shocks approach the corner as is the case in Figure 9(c) and reflect from it, there is a slight gap along the centreline of the nozzle; now if the shock waves are strong enough they will bridge this gap and form a uniform front that has the ability to withstand the high-speed opposing flow that is simultaneously entering the test section. But due to the relatively weak shock strength of the lower driver pressure, this front dissipates.

The supersonic air exiting the nozzle results in the generation of oblique shock structures at the two higher driver pressures in Figures 7(c) and 8(c). As time goes by and the morphological shock structures move further downstream into the ejector, a chain of small vortices begins to form at the location of the shear layers. These are formed once the fluid through the uniform area section encounters the area change and begins to form a 'starting jet'.[54] The formation of the starting jet gives rise to these vortices generated due to the formation of a shear layer between emerging and external fluids. This is best illustrated in Figure 7(d).

Each time a new wave diffracts into the open area channel and travels towards the ejector walls, it first passes the preceding waves which have already been reflected from the walls and this leads to the creation of more cross-overs both in the positive and negative flow directions. The reflected waves, from the upper and lower ejector walls, travel towards the centre of the model and interact with the vortex cores. As already mentioned, the reflected shocks that interact with the vortex cores go through shock splitting. As a result, they are separated from the rest of the flow and generate standing shock waves above and below the turbulent region in the centre of the model. These shocks can be seen in Figures 7(d) and 8(d) but do not exist for the diaphragm pressure ratio of 4. The turbulent region along the centre of the model is created due to the dissipation of the vortex cores.

F. Pressure Measurements

The pressure history along the side wall for all five transducers is shown in Figure 10(a) for the case of $P_4/P_1 = 12$ during the total run time of the shock tube, and in Figure 10(b) for the first 10 ms of the flow. The pressure traces of $P_4/P_1 = 4$ and 8 appear qualitatively similar, and vary only in magnitude. Examining closely these plots we can pin point interesting features that correlate with the shadowgraphs. The pressure oscillation of transducers $T1$ and $T2$ in Figure 10(b), after the passage of the incident shock wave, are due to the passage of the focused shock structures. Since the transducers are placed along the centreline of the nozzle, it would be reasonable to assume that each pressure variation corresponds to a focal point. The oscillations of transducer $T3$ are more frequent, due to the consecutive shock reflections from the upper and lower walls of the uniform area channel.

To understand better the pressure variation of transducers $T4$ and $T5$ along the side wall, we must refer back to Figures 6 and 8. The first pressure changes recorded by these transducers are due to the diffracted precursor shock front and the multiple waves that follow it. These fluctuations are more intense and also more frequent at the higher pressure ratio. This is also evident if we compare the shadowgraphs of Figures 6(d) and 8(a). The pressure fluctuations of transducer $T5$ are more pronounced compared to transducer 4. Since transducer $T5$ is placed approximately 40 mm downstream of transducer $T4$, this gives the flow more time to generate more reflected waves from the ejector walls leading to higher compression. The interaction between the turbulent vortical region in the middle of the test section and the reflected shocks from the ejector walls, gives rise to the fluctuating pressure profiles of transducers $T4$ and $T5$, especially at higher flow Mach numbers due to the severity of the interaction.

In Figure 10(a), the arrival of the original incident shock wave is the first phenomenon captured by the transducers. As is expected, the arrival time varies for the different pressure ratios; it occurs after 3.50 ms, 3.10 ms, and 2.85 ms for driver pressure ratios of 4, 8 and 12, respectively. The first two transducers seem to have a gradual pressure increase until a first maximum (A), a reduction (B) and afterwards increase again (C).

The pressure rise A is due to the upstream travelling flow which fills the shock tube. Due to the depletion of pressurised air, the pressure drops to B until the initially upstream travelling waves reflect from the shock tube end wall and move into the area convergence,

which cause the pressure to increase to point C. As the air depletes from the shock tube, the pressure gradually approaches ambient. Table I provides the percentage drop in pressure as a result of the aforementioned flow behaviour for the different diaphragm pressure ratios.

The PDE operation is controlled by three time periods, one of which is the purging period, τ_{purge}, during which a small amount of cold air is injected to prevent preignition of fresh reactants.[58] The pressure within the chamber must not be higher than the stagnation pressure of the inlet air to allow for purging and refilling. Therefore, the pressure rise caused by the upstream travelling flow plays an important role in the optimum performance of multi-cycle PDEs.

As the flow along the centreline travels downstream and begins to dissipate, the pressure traces of transducers $T4$ and $T5$ show an oscillation of pressure due to the separation of the boundary layer formed on the side wall. The separation of the boundary layer is caused by the passage of the vortical field that originated from the exit of the uniform area section. For the 12 *bar* driver pressure, these effects are more pronounced in the pressure history due to the greater momentum of the flow. These oscillations are below atmospheric, and as the driving force which is the expanded flow from the driver section diminishes, the pressure gradually approaches ambient.

Figure 11 shows the pressure history of transducers $T6$ and $T7$, placed along the lower wall of the ejector. The reason for choosing these two locations, is to capture the regular and Mach reflection of the diffracted shock front. In Figure 11(a), the first pressure change corresponds to the passage of the precursor shock wave that has gone through a regular reflection at this point. The magnitude of this change is greater and occurs earlier at higher driving pressures. The precursor shock is quickly followed by, depending on the driving pressure, a number of diffracted shocks that also have a regular reflection pattern upon collision with the wall. These secondary diffracted waves originate from the constant area channel (Sect. III C).

The passage of the precursor reflected wave from the location of the transducer gives rise to two features; firstly, an increase of pressure due to its arrival[59] and secondly, a decrease in pressure due to the expansion of the flow as a result of the reflected shock moving away from the wall towards the centre of the section and also the simultaneous movement of the flow downstream.[35]

The pressures corresponding to the passage of the Mach stem given in Figure 11(b) are

higher compared to the regular reflection. This is due to the fusion between the incident and the reflected waves resulting in a stronger front which is normal to the surface. The effect of the continuous shock passages becomes weaker as the shocks travel downstream, since the volume of air expanding from the shock tube, which acts as the driving force, vanishes.

The pressure history for total run time of the transducers shown in Figure 11 is presented in Figure 12. It can be seen that the directed flow into the ejector causes a significant vacuum pressure on the ejector wall (Figure 12(a)); at higher shock tube driver pressures, the inlet suction increases. The increase in static pressure of transducer 7 in Figure 12(b) is attributed to mixing as the flow travels through the ejector and the pressure gradually approaches ambient.

IV. CONCLUSIONS

A two-dimensional air-ejector system, with incident shock waves generated using a shock tube having diaphragm pressure ratios of $P_4/P_1 = 4$, 8, and 12 has been investigated. The test section allows for the study of many compressible flow elements: shock reflections, both regular and irregular (Mach reflection), vortex generation, shock/vortex interaction, and shock diffraction. The combination of these features gives rise to a complex flowfield that has been studied qualitatively by shadowgraphy and quantitatively by means of pressure measurements. Perhaps a feature that has not been documented before, as far as the authors are aware, is the merger of two reflected shocks at their ends which gave rise to a single front propagating into oncoming flow. This only occurred at the two higher driving pressures. In multi-cycle PDEs, the combustion products must be purged after the first cycle in order for the nozzle to remain effective, and the effects of the upstream travelling flow become important.

Side wall pressure measurements at the nozzle inlet, indicated the cumulative pressure rise each time a shock focus passes. For each focal point present in the convergent section, a diffracted wave was generated; this was due to the continuous reflection of the shocks within the uniform area section at the nozzle exit. Upon collision with the confined walls of the chamber the diffracted waves underwent regular reflection with transition to irregular reflection further downstream. The pressure as a result of the passage of the Mach stem was shown to be higher than the regular reflection case. This is due to the fusion between the

incident and reflected waves.

An embedded or diaphragm shock is formed due to the existence of a locally supersonic flow and balances the higher back pressure at the nozzle exit. The stability of this shock is greatly influenced by the surrounding flow. Since the chamber is a confined one, the successive reflections of the diffracted shocks from the ejector walls continuously bombard the flow phenomena created along the model centre; these include the primary vortex cores, the sheet of subvortices generated behind them and the diaphragm shock.

Pressure-sensitive paint (PSP) studies will be conducted to provide global pressure data on the side wall of the test section, and these will be compared with the shadowgraph and discrete pressure data presented in the current paper. This will provide more quantitative data for the process of design optimisation.

Acknowledgments

The authors thank Shimadzu, UK branch, for the loan of their Hypervision camera and for the technical assistance of Lorna Moffatt and Dr. Johannes Hesper. The continuous support of Dr. D. Kounadis and the technical staff at The University of Manchester is very much appreciated. The funding of EPSRC is also acknowledged.

[1] Ben-Dor G., Takayama K., and Dewey J.M., "Further analytical considerations of weak shock wave reflections over a concave wedge," *Fluid Dynamics Research*, Vol. 2, 1987, pp. 77–85.

[2] Ben-Dor G., and Takayama K., "The dynamics of the transition from Mach to regular reflection over concave cylinders," *Israel Journal of Technology*, Vol. 2, 1986/7, pp. 71–74.

[3] Henderson L.F., and Lozzi A., "Experiments on transition of Mach reflexion," *Journal of Fluid Mechanics*, Vol. 68, 1975, pp. 139–155.

[4] Skews B.W., "The shape of a diffracted shock wave," *Journal of Fluid Mechanics*, Vol. 29, 1967, pp. 705–719.

[5] Skews B.W., "The perturbed region behind a diffracting shock wave," *Journal of Fluid Mechanics*, Vol. 29, 1967, pp. 297–304.

[6] Griffith, W., and Brickl, D.E., "The diffraction of strong shock waves," *Physical Review*, Vol. 2, 1952, pp. 451–453.

[7] Chang, K.S., and Kim, J.K., "Numerical investigation of inviscid shock wave dynamics in an expansion tube," *Shock Waves*, Vol. 5, 1995, pp. 33–45.

[8] Jiang, Z., Takayama, K., Babinsky, H., and Meguro, T., "Transient shock wave flows in tubes with a sudden change in cross section," *Shock Waves*, Vol. 7, 1997, pp. 151–162.

[9] Shepherd, J.E., Schultz, E., and Akbar, R., "Detonation diffraction," *Proceedings of the 22nd International Symposium on Shock Waves*, 1999.

[10] Edwards, D.H., Thomas, G.O., and Nettleton, M.O., "The diffraction of a planar detonation wave at an abrupt area change," *Journal of Fluid Mechanics*, Vol. 95, 79–96 (1979).

[11] Jones, D.A., Sichel, M., and Oran, E.S., "Reignition of detonations by reflected shocks," *Shock Waves*, Vol. 5, 1995, pp. 47–57.

[12] Pantow, E.G., Fischer, M., and Kratzel, T., "Decoupling and recoupling of detonation waves associated with sudden expansion," *Shock Waves*, Vol. 6, No. 3, 1996, pp. 131–137.

[13] Papalexandris, M.V., Thomas, J.F., Jacobs, C., and Deledicque, V., "Structural characteristics of detonation expansion from a small channel to a larger one," *Proceedings of the Combustion Institute*, 2007, pp. 2407–2414.

[14] Ma, F., Choi, J.Y., and Yang, V., "Thrust chamber dynamics and propulsive performance of single-tube pulse detonation engines," *Journal of Propulsion and Power*, Vol. 21, No. 3, 2005,

pp. 512–526.

[15] Oh, J.Y., Ma, F., Hsieh, S.Y., and Yang, V., "Interactions between shock and acoustic waves in a supersonic inlet diffuser," *Journal of Propulsion and Power*, Vol. 21, No. 3, 2005, pp. 486–495.

[16] Ohyagi, S., Obara, T., Hoshi, S., Cai, P., and Yoshihashi, T., "Diffraction and re-initiation of detonations behind a backward-facing step," *Shock Waves*, Vol. 12, 2002, pp. 221–226.

[17] Glaser, A.J., Caldwell, N., Gutmark, E., Hoke, J., Bradley, R., and Schauer, F., "Effects of tube and ejector geometry on the performance of pulse detonation engine driven ejectors," *42nd AIAA/ASME/SAE/ASEE Joint Propulsion Conference & Exhibit, California*, AIAA Paper 2006-4790, 2006.

[18] Wilson, J., Sgondea, A., Paxson, D.E., and Rosenthal, B.N., "Parametric investigation of thrust augmentation by ejectors on a pulsed detonation tube," *Journal of Propulsion and Power*, Vol. 23, No. 1, 2007, pp. 108–115.

[19] Kailasanath, K., "Recent developments in the research on pulse detonation engines," *AIAA Journal*, Vol. 41, No. 2, 2003, pp. 145–159.

[20] Glaser, A.J., Caldwell, N., Gutmark, E., Hoke, J., Bradley, R., and Schauer, F., "Experimental study of ejectors driven by a pulse detonation engine," *45th AIAA Aerospace Sciences Meeting and Exhibit, Reno*, AIAA Paper 2007-447, 2007.

[21] Ma, F., Choi, J.Y., and Yang, V., "Propulsive performance of airbreathing pulse detonation engines," *Journal of Propulsion and Power*, Vol. 22, No. 6, 2006, pp. 1188–1203.

[22] Allgood, D., Gutmark, E., Rasheed, A., and Dean, A.J., "Experimental investigation of a pulse detonation engine with a two-dimensional ejector," *AIAA Journal*, Vol. 43, No. 2, 2005, pp. 390–398.

[23] Yungster, S., "Analysis of nozzle and ejector effects on pulse detonation engine performance," *41st AIAA Aerospace Sciences Meeting and Exhibit, Reno*, AIAA Paper 2003-1316, 2003.

[24] Glaser, A.J., Caldwell, N., Gutmark, E., "A fundamental study on acoustic behavior of pulsed detonation engines," *45th AIAA Aerospace Sciences Meeting and Exhibit, Reno*, AIAA Paper 2007-444, 2007.

[25] Kontis, K., An, R., Zare-Behtash, H., and Kounadis, D., "Head-on collision of shock wave induced vortices with solid and perforated walls," *Physics of Fluids*, Vol. 20, 2008, pp. 1–17.

[26] Kontis, K., An, R., and Edwards, J., "Compressible vortex-ring interaction studies with a number of generic body configuration," *AIAA Journal*, Vol. 44, No. 3, 2006, pp. 2962–2978.

[27] Zare-Behtash, H., Kontis, K., and Takayama, K., "Compressible vortex loops studies in a shock tube with various exit geometries," *46th AIAA Aerospace Sciences Meeting and Exhibit, Reno*, AIAA Paper 2008-0362, 2008.

[28] Eustace, V.A., "A study of two-dimensional supersonic air ejector systems," *PhD Thesis*, The University of Manchester Institute of Science and Technology, 1969.

[29] Zare-Behtash, H., Gongora, N., Lada, C., Kounadis, D., and Kontis, K., "Shock Wave Interactions Inside A Complex Geometry," *26th International Symposium on Shock Waves (ISSW26) Goettingen, Germany*, 2007.

[30] Settles, G.S., "Schlieren and Shadowgraph Techniques," *Springer Verlag*, 2001.

[31] Bynum, D.S., Ledford, R.L., and Smotherman, W.E., "Wind tunnel pressure measuring techniques," *AGARD report, AGARD-AG-145-70*, 1970.

[32] Kline, S.J., and McClintock, F.A., "Describing Uncertainties in Single-Sample Experiments," *Journal of Mechanical Engineering*, Vol. 75, 1953, pp. 3–7.

[33] Chisnell, R.F., "The motion of a shock wave in a channel, with applications to cylindrical and spherical shock waves," *Journal of Fluid Mechanics*, Vol. 2, 1957, pp. 286–298.

[34] Bird, G.A., "The effect of wall shape on the degree of reinforcement of a shock wave moving into a converging channel," *Journal of Fluid Mechanics Digital Archive*, Vol. 5, 1959, pp. 60–66.

[35] Sloan, S.A., and Nettleton, M.A., "A model for the decay of a wall shock in a large abrupt area change," *Journal of Fluid Mechanics*, Vol. 88, 1978, pp. 259–272.

[36] Russell, D.A., "Shock-wave strengthening by area convergence," *Journal of Fluid Mechanics*, Vol. 27, 1967, pp. 305–314.

[37] Korobeinikov, V.P. "Unsteady Interaction of Shock and Detonation Waves in Gases," *Hemisphere Publishing Corporation*, 1989.

[38] Ben-Dor, G., "Shock Wave Reflection Phenomena," *Springer-Verlag*, 1992.

[39] Hornung, H.G., "Oblique shock reflection from an axis of symmetry," *Journal of Fluid Mechanics*, Vol. 409, 2000, pp. 1–12.

[40] Sturtevant, B., and Kulkarny, V.A., "The focusing of weak shock waves," *Journal of Fluid Mechanics*, Vol. 73, 1976, pp. 651–672.

[41] Hillier, R., "Computation of shock wave diffraction at a ninety degrees convex edge," *Shock Waves*, Vol. 1, 1991, pp. 89–98.

[42] Bazhenova, T.V., Gvozdeva, L.G., and Zhilin, Yu. V., "Change in the shape of the diffracting

shock wave at a convex corner," *Acta Astronautica*, Vol. 6, 1979, pp. 401–412.

[43] Sloan, S.A., and Nettleton, M.A., "A model for the axial decay of a shock wave in a large abrupt area change," *Journal of Fluid Mechanics*, Vol. 71, 1975, pp. 769–784.

[44] Sun, M., and Takayama, K., "Vorticity production in shock diffraction," *Journal of Fluid Mechanics*, Vol. 478, 2003, pp. 237–256.

[45] Barkhudarov, E.M., Mdivnishvili, M.O., Sokolov, I.V., Taktakishvili, M.I., and Terekhin, V.E., "Mach reflection of a ring shock wave from the axis of symmetry," *Journal of Fluid Mechanics*, Vol. 226, 1991, pp. 497–509.

[46] Kobayashi, S., Adachi, T., and Suzuki, T., "Examination of the von Neumann paradox for a weak shock wave," *Fluid Dynamics Research*, Vol. 17, 1995, pp. 13–25.

[47] Ben-Dor, G., and Takayama, K., "The phenomena of shock wave reflection - a review of unsolved problems and future research need," *Shock Waves*, Vol. 2, 1992, pp. 211–223.

[48] Olim, M., and Dewey, J.M., "A revised three-shock solution for the Mach reflection of weak shocks ($1.1 < M_i < 1.5$)," *Shock Waves*, Vol. 2, 1992, pp. 167–176.

[49] Sakurai, A., Henderson, L.F., Takayama, K., Walneta, Z., and Colella, P., "On the von Neumann paradox of weak Mach reflection," *Fluid Dynamics Research*, Vol. 4, 1989, pp. 333–345.

[50] Kontis, K., Kounadis, D., An, R., and Zare-Behtash, H., "Vortex ring interaction studies with a cylinder and a sphere," *International Journal of Heat and Fluid Flow*, Vol. 29, 2008, pp. 1380–1392.

[51] Baird, J.P., "Supersonic vortex rings," *Proceedings of the Royal Society of London. Series A.*, Vol. 409, 2005, pp. 59–65.

[52] Minota, T., "Dynamic motion of a compressible vortex ring," *Proceedings of the SPIE-The International Society for Optical Engineering*, Vol. 3173, 1997, pp. 241–248.

[53] Broadbent, E.G., and Moore, D.W., "The interaction of a vortex ring and a coaxial supersonic jet," *Proceedings of the Royal Society of London. Series A*, Vol. 409, 1987, pp. 47–57.

[54] Abate, G., and Shyy, W., "Dynamic structure of confined shocks undergoing sudden expansion," *Progress in Aerospace Sciences*, Vol. 38, 2002, pp. 23–42.

[55] Ellzey, J.L., Henneke, M.R., Picone, J.M., and Oran, E.S., "The interaction of a shock with a vortex: Shock distortion and the production of acoustic waves," *Physics of Fluids*, Vol. 1, 1995, pp. 172–184.

[56] Chatterjee, A., "Shock wave deformation in shock-vortex interactions," *Shock Waves*, Vol. 9,

1999, pp. 95–105.

[57] Keller, J., and Merzkirch, W., "Interaction of a normal shock wave with a compressible turbulent flow," *Experiments in Fluids*, Vol. 8, 1990, pp. 241–248.

[58] Wu, Y., Ma, F., and Yang, V., "System performance and thermodynamic cycle analysis of airbreathing pulse detonation engines," *Journal of Propulsion and Power*, Vol. 19, No. 4, 2003, pp. 556–567.

[59] von-Neumann, J., "John von Neumann Collected Works, The Mach effect and height of burst," *Pergamon Press*, 1963.

TABLE I: Transducer T2 pressure variation (see Fig.10)

P_{ratio}	1^{st} $P_{max}[bar]$	% P_{drop}	2^{nd} P_{max}[bar]
4	1.24	9.11	1.18
8	1.52	10.53	1.47
12	1.77	10.28	1.72

List of Figures

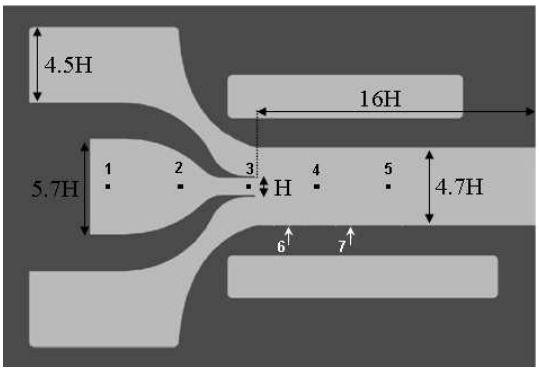

FIG. 1: Schematic diagram of the shock tube test section (where $H = 9.6mm$).

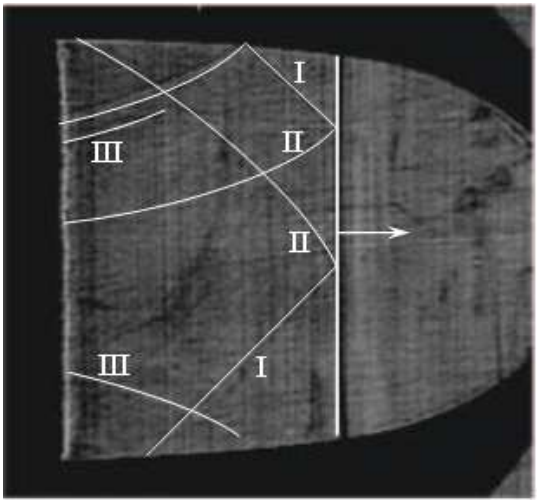

(a)

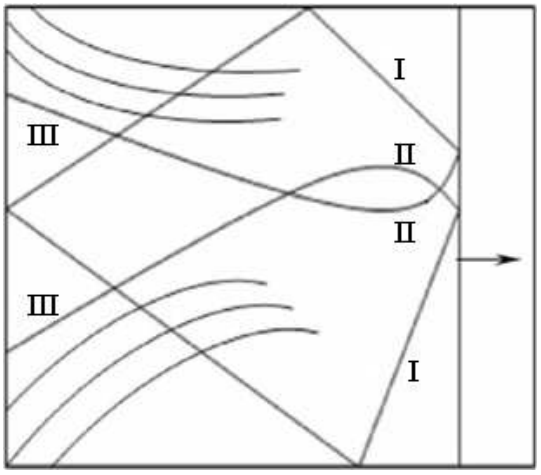

(b)

FIG. 2: Flow features in the convergent concave section for $P_4/P_1 = 8$, a) shadowgraph, b) schematic of the observed flow features.

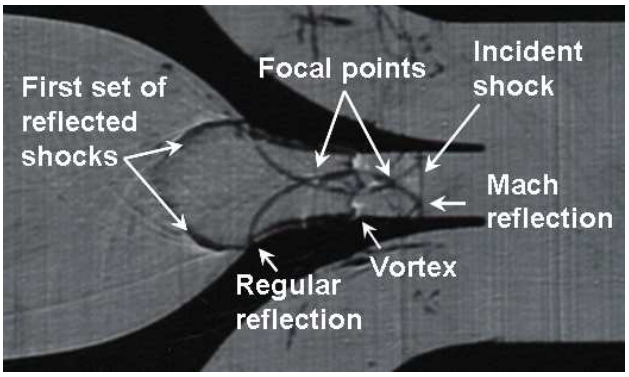

FIG. 3: Flow pattern in the constant-area section, $P_4/P_1 = 12$.

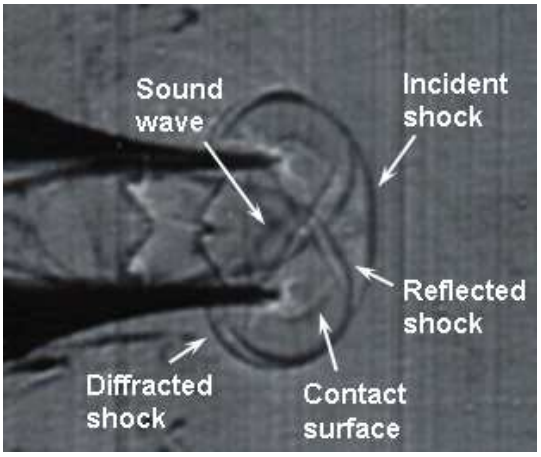

(a)

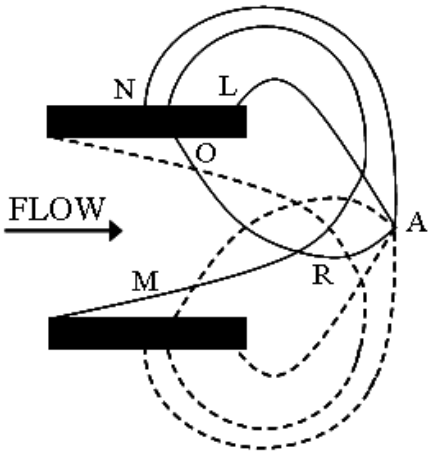

(b)

FIG. 4: Shock diffraction for $P_4/P_1 = 8$, a) shadowgraph, b) schematic of the diffracted flow field.

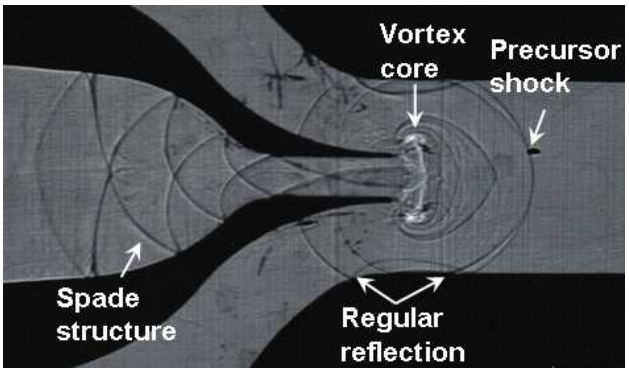

FIG. 5: Shock diffraction into the open-area section.

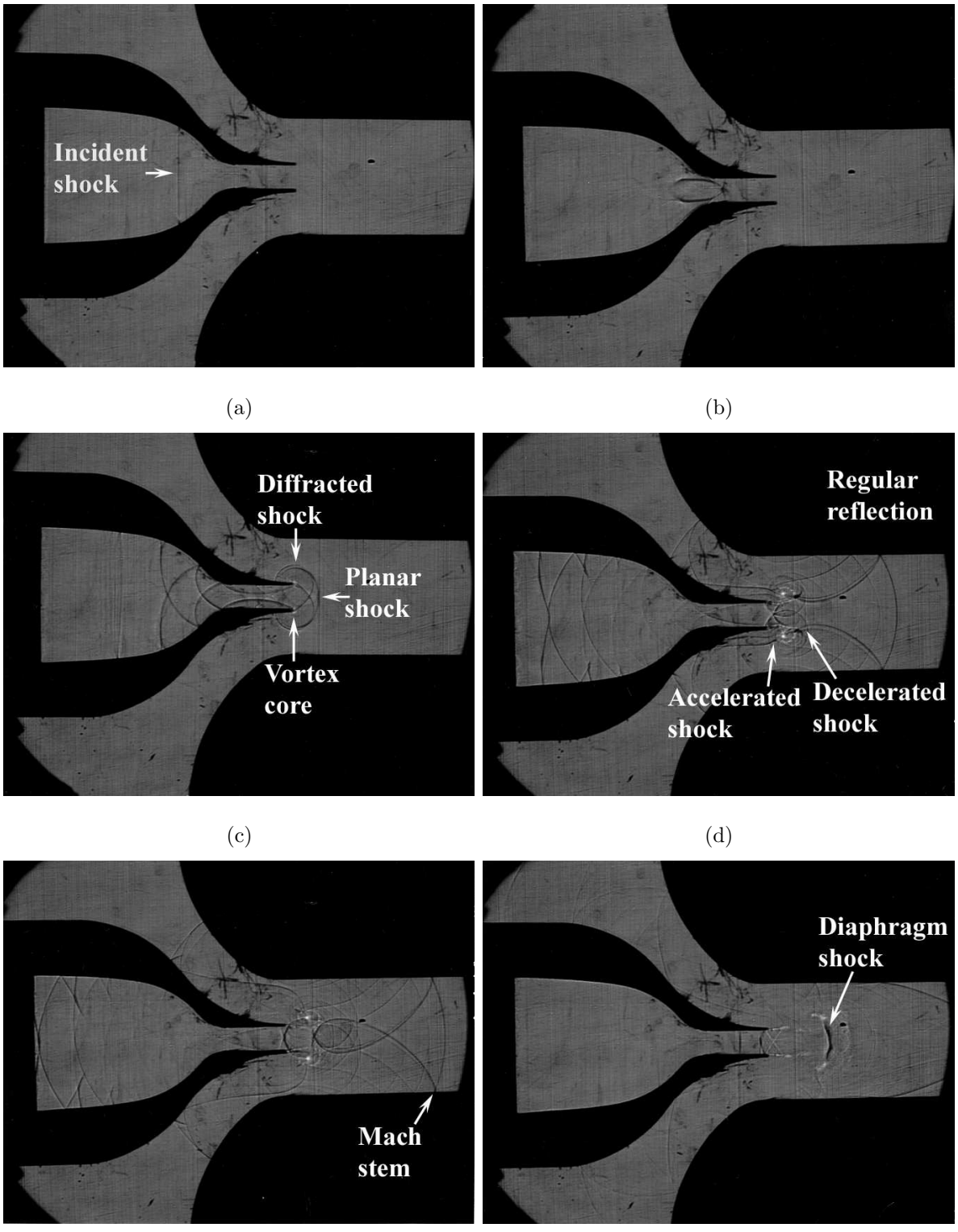

FIG. 6: Time-resolved shadowgraphs for diaphragm pressure ratio of $P_4/P_1 = 4$. a) 0 ms, b) 0.06 ms, c) 0.12 ms, d) 0.20 ms, e) 0.27 ms, f) 0.42 ms.

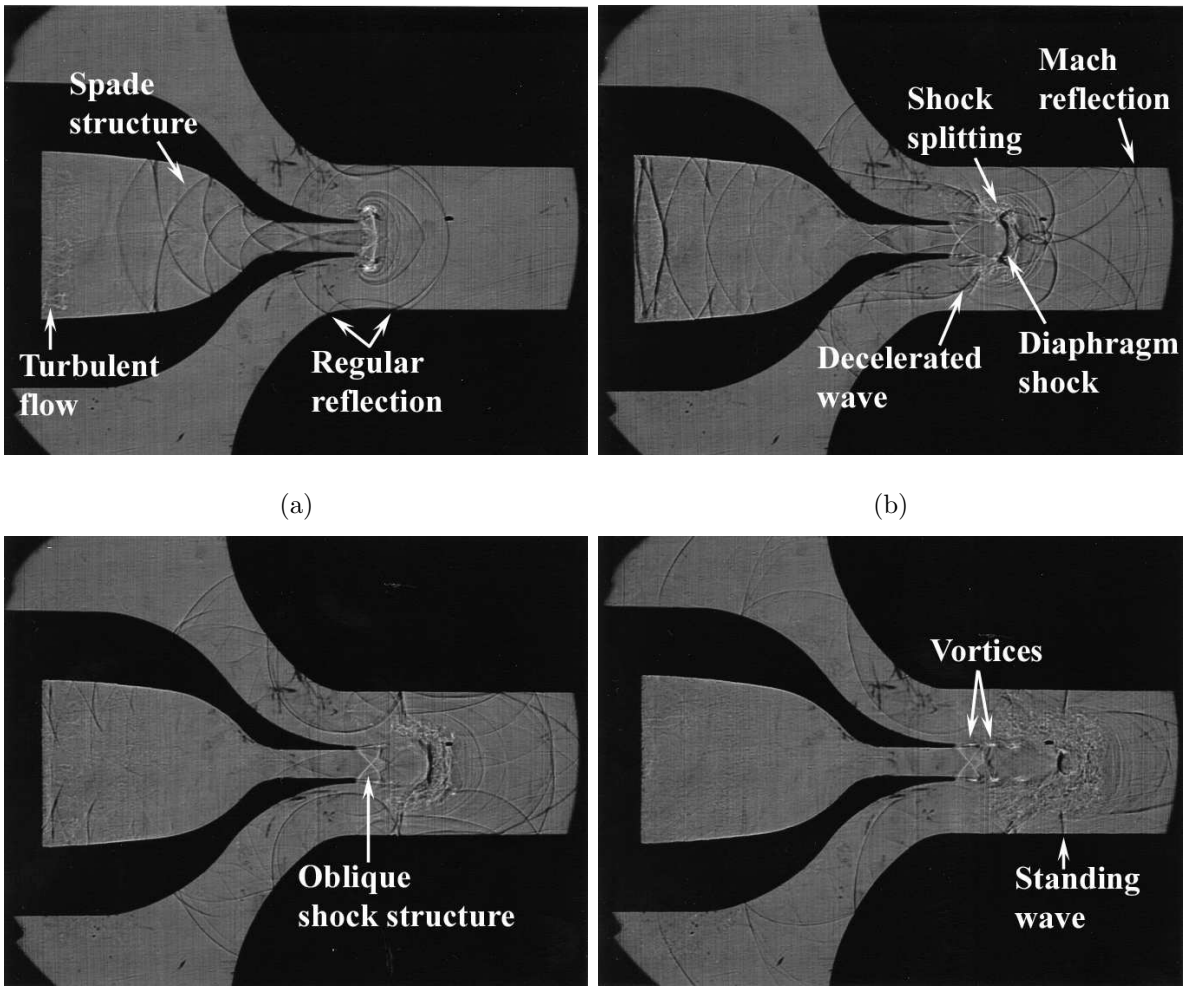

FIG. 7: Time-resolved shadowgraphs for diaphragm pressure ratio of $P_4/P_1 = 8$. a) 0.13 ms, b) 0.22 ms, c) 0.26 ms, d) 0.37 ms.

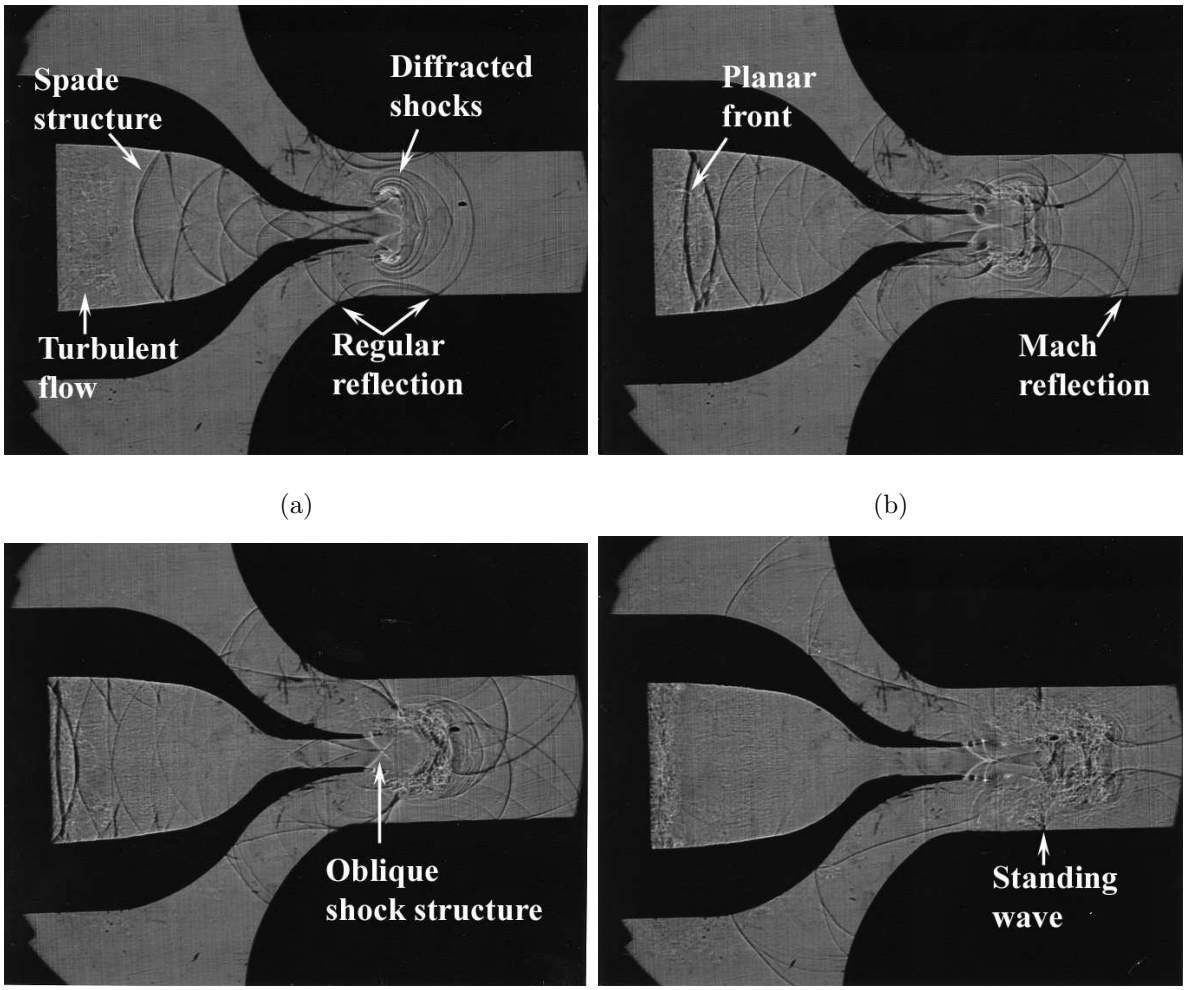

(a) (b)

(c) (d)

FIG. 8: Time-resolved shadowgraphs for diaphragm pressure ratio of $P_4/P_1 = 12$. a) 0.12 ms, b) 0.19 ms, c) 0.21 ms, d) 0.29 ms.

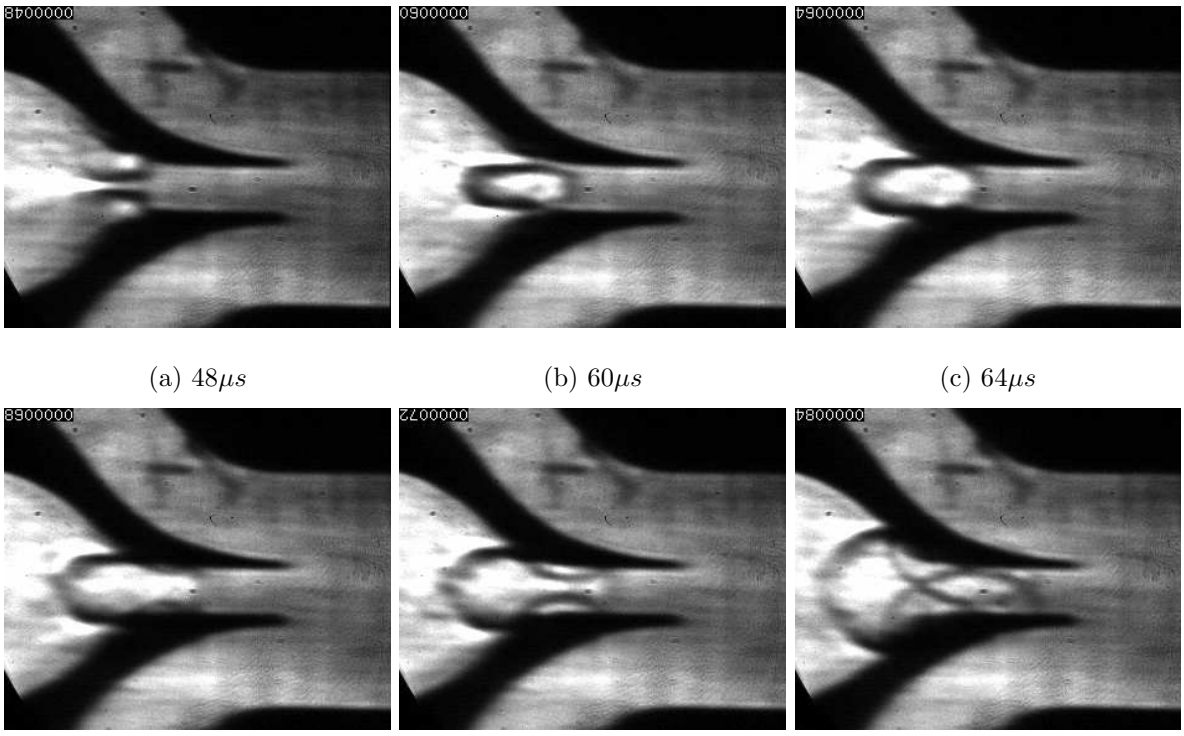

(a) $48\mu s$ (b) $60\mu s$ (c) $64\mu s$

(d) $68\mu s$ (e) $72\mu s$ (f) $84\mu s$

FIG. 9: Formation of the precursor spade structure for diaphragm pressure ratio of $P_4/P_1 = 8$.

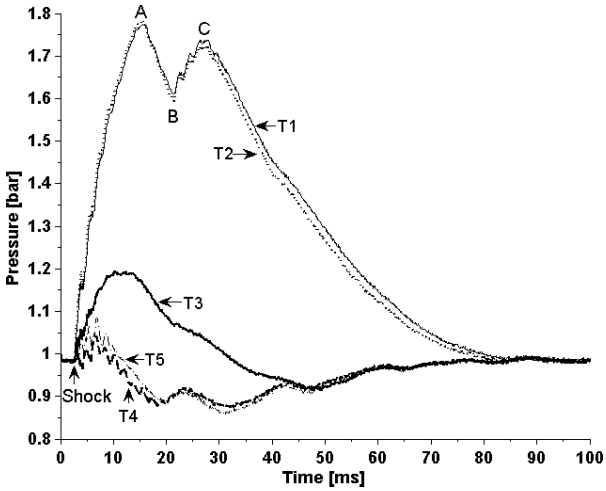

(a)

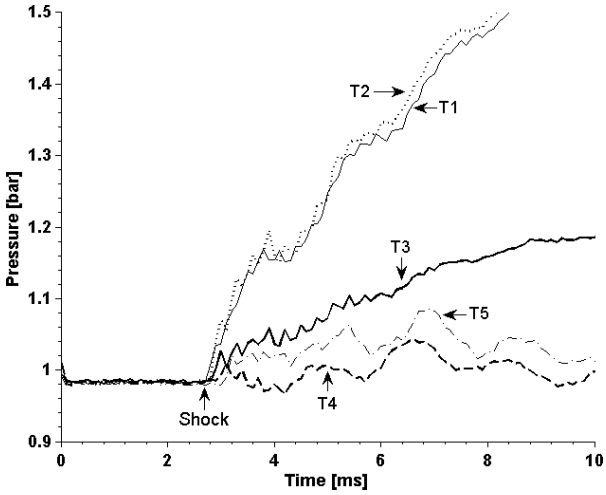

(b)

FIG. 10: Pressure history along the side wall. $P_4/P_1 = 12$, (a) total run time, (b) first 10 ms of measurement. $T1 = 10\ mm$, $T2 = 50\ mm$, $T3 = 90\ mm$, $T4 = 130\ mm$, $T5 = 170\ mm$. Transducer locations are depicted in Figure 1.

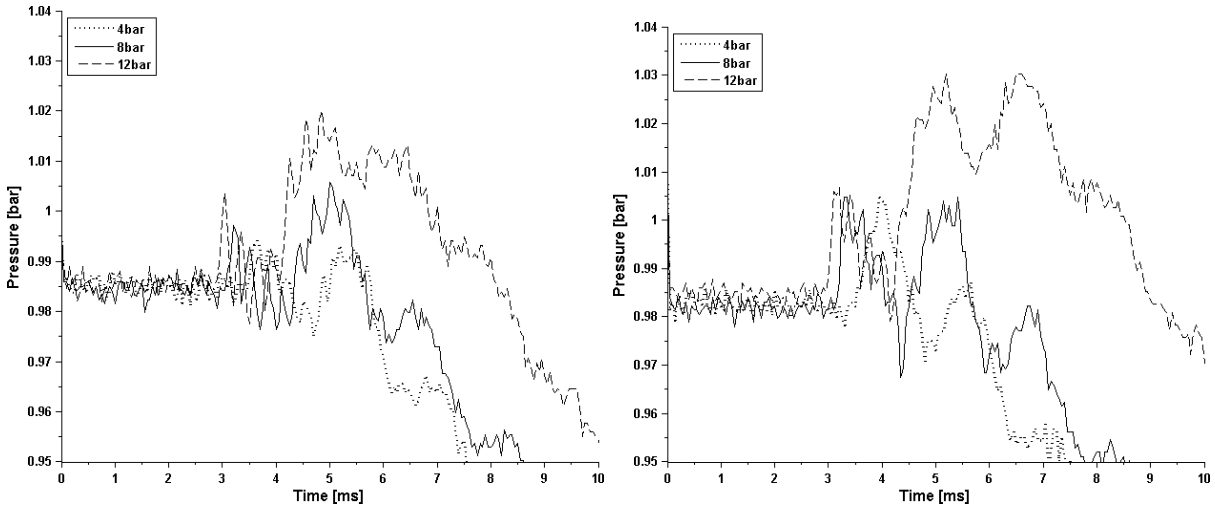

(a) (b)

FIG. 11: Pressure history for the first 10 ms of measurement, for: (a) transducer 6, (b) transducer 7, on the ejector bottom wall for different driver pressures.

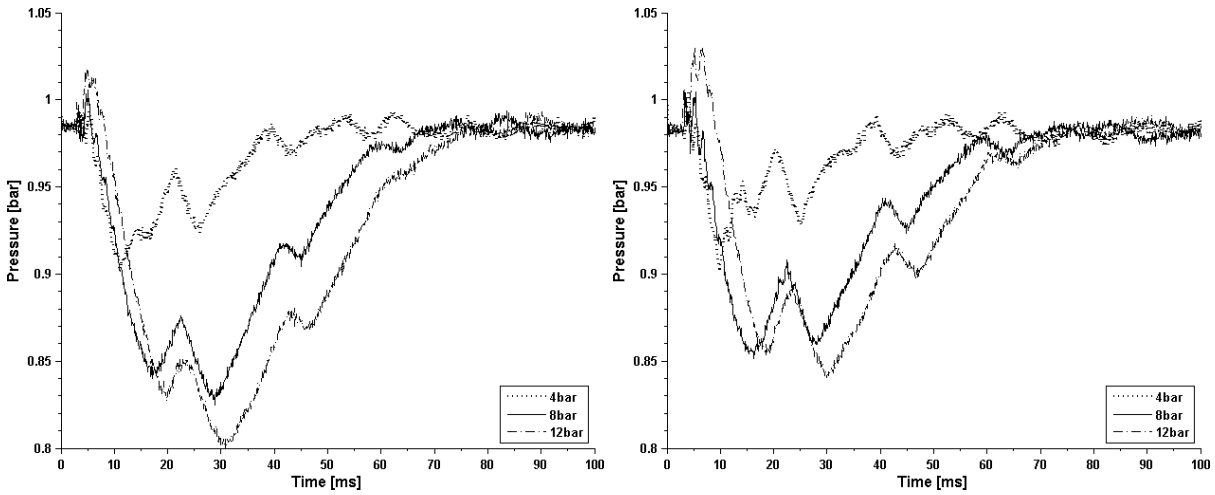

(a) (b)

FIG. 12: Pressure history for the total run time, (a) transducer 6, (b) transducer 7, on the ejector bottom wall for different driver pressures.